Transp Porous Med (2014) 101:81–97
DOI 10.1007/s11242-013-0232-0

CT Imaging of Low-Permeability, Dual-Porosity Systems Using High X-ray Contrast Gas

Bolivia Vega · Abhishek Dutta · Anthony R. Kovscek

Received: 18 March 2013 / Accepted: 18 September 2013 / Published online: 3 October 2013

Abstract Low-permeability, dual-porosity media such as coal and gas shale (i.e., mudstone) exhibit structural and chemical features across a range of scales spanning from tens of meters to nanometers. Characterization methods and efforts for these porous media are needed to understand gas in place, gas flow behavior, and storage capacity for potential CO_2 sequestration. Characterizing the structure and heterogeneity of representative samples helps determine how the physical and chemical processes associated with CO_2 transport in coal and gas shale affect injectivity and storage capacity (over long periods of time), and the ability of these media to sequester CO_2 (as both a free and adsorbed phase) for thousands of years. In this study, an imaging technique focused on the submillimeter scale is applied to shale and coal samples of interest. In particular, porosity, component matrix distribution, and evidence of gas transport through these tight media were studied.

Keywords Mudstone · Gas shale · X-ray imaging · Core analysis

1 Introduction

In this study, Barnett, Eagle Ford, and Haynesville gas shale and Powder Basin coal samples were studied. The pore structure of these samples was investigated using xenon and krypton as high-contrast gases injected and monitored with an X-ray computed tomography (CT) technique that enables the visualization of porosity and fracture networks, as well as gas transport, in the case of coal.

X-ray computed tomography has emerged as an important and powerful tool for nondestructive imaging because it is relatively easy and flexible to apply, offers fine spatial resolution, and is adaptable to many types of experimental procedures and flow conditions (Akin and Kovscek 2003). Using imaging techniques, the distribution of bulk density,

B. Vega · A. Dutta · A. R. Kovscek (✉)
Energy Resources Engineering, Stanford University, Stanford, CA, USA
e-mail: kovscek@stanford.edu

fractures, and volumetric strain fraction can be defined and used to understand flow characteristics of gas in these naturally fractured, dual-porosity reservoirs (Saites et al. 2006).

In general, gas-bearing low-permeability porous media such as gas shale and coal have been largely overlooked or postponed as a viable energy resource. Lack of motivation to produce them in the fossil fuel energy market and their inherent heterogeneous and anisotropic nature pushed them to the far background of the energy resources inventory. Efforts to characterize and model their dual-porosity structure and stress-dependent permeability were relegated to lower priority.

The advent of new drilling and completion technologies such as horizontal drilling and hydraulic fracturing (Curtis et al. 2011), a growing network of natural gas pipelines and specialized ships to carry LNG, depleting oil reserves, and strict anti-flaring regulations have made natural gas production easier and more attractive. The USA is one of the major producers of natural gas with an annual production of 25.69 TCF in 2012, and the gas shale contribution to US dry gas production was about 35 % of total US dry production (DOE, www.eia.gov)

Additionally, fossil fuels are the conventional sources of energy, and their widespread consumption has led to emission of greenhouse gases. One of the methods to reduce carbon dioxide (CO_2) concentration in the atmosphere is by sequestering it in geological formations such as depleted oil reservoirs and saline aquifers (IPCC 2005). To improve economic viability, geological sequestration activities should be considered in conjunction with enhanced recovery of oil and natural gas. Gas shale and coalbeds are emerging as potential options for subsurface sequestration of anthropological carbon dioxide because of their capability to store free and sorbed gas, presumably within their organic component.

Shale is a clastic, sedimentary mudstone that is composed of a mixture of fine-grained inorganic material including mud, clay, pyrite, and silica, as well as, potentially, organic material. Shales are relatively low porosity and ultra-low permeability with pore sizes ranging from the order of nm's to 100's of nm with fracture apertures being potentially much greater. Thus, there is a wide arrangement of sizes through which fluids flow and a multi-modal pore distribution (Akkutlu and Fathi 2011). A large number of studies (Lu et al. 1992; Wang and Reed 2009; Kang et al. 2010; Akkutlu and Fathi 2011; Sondergeld et al. 2010; Ambrose et al. 2010) agree that at the nanoscale, mostly interconnected organic pores located in the kerogen component of the shale rock are responsible for gas sorption. Because of its direct relationship with storage ability, gas shale porosity is the topic of many of these and other studies. It has been demonstrated that CO_2 is preferentially sorbed in organic-rich shales relative to CH_4 (Nuttall et al. 2005). In the case of shales, sorption occurs on both the organic constituents and the clays. Development for natural gas utilizes wells and other infrastructure that is being constructed for shale gas production. Accordingly, the potential for using organic-rich shale formations with prebuilt infrastructure for CO_2 sequestration is particularly attractive.

A similar process occurs in coal and is the basis for enhanced coalbed methane recovery and geologic sequestration of CO_2 in unmineable coal seams. Enhanced coalbed methane (ECBM) recovery by injection of CO_2 or mixtures of CO_2 and N_2 to mitigate permeability reduction are potential methods to recover additional natural gas while at the same time sequestering CO_2 in the subsurface (Jessen et al. 2008; Lin et al. 2008). Storage of CO_2 in coal seams is a potentially attractive carbon sequestration technology because it enhances methane (natural gas) production from coalbeds as well as has the potential to be carbon neutral and perhaps a carbon sink (Wong et al. 2000; Harris et al. 2008). In some cases, this can be cost effective as the additional CH_4 recovery from coal can either partially or completely offset the operational costs incurred.

2 X-ray CT Imaging

CT scanning is a nondestructive imaging technique that provides two- and three-dimensional images of opaque objects. It is relatively easy to apply, offers fine spatial resolution, and is adaptable to many types of experimental procedures.

In this study, the object of interest is placed inside a circular array of X-ray detectors and a single X-ray source rotates around the sample. Because the X-ray tube moves around the apparatus in a circular path and reconstruction algorithms assume symmetric objects, images display fewer artifacts when the scanned object has a circular cross section (e.g., Le Guen and Kovscek 2006). After the image is reconstructed, the computer converts the measured attenuation into CT (dimensionless Hounsfield) units normalized to the linear attenuation coefficient of water. Each Hounsfield unit represents a 0.1 % change in density with respect to the calibration density scale. By definition, the CT numbers of air and water are −1,000 and 0, respectively. Akin and Kovscek (2003) provide a comprehensive review.

Early adopters of CT imaging to rock characterization in the oil industry (Honarpour et al. 1985; Vinegar and Wellington 1987; Whithjack 1988) offered reports on the measurements of rock properties such as porosity and flow visualization for a range of studies. Whithjack 1988 performed CT porosity measurements from two scans at the same location(s) of the sample under two different saturating fluids as

$$\frac{\mathrm{CT}_{1r} - \mathrm{CT}_{2r}}{\mathrm{CT}_1 - \mathrm{CT}_2} \tag{1}$$

where the subscripts 1 and 2 represent the saturating fluids, and normally, these are water and air, respectively. The subscripts $1r$ and $2r$, in turn, represent the CT numbers of rock saturated with fluids 1 and 2, respectively. Whithjack et al. (2003) later compiled a report on the most widely used applications of CT scan technology.

With CT scan imaging, there is a trade-off between the spatial resolution and the sample size. Sample size is generally two to three orders of magnitude greater than the resolution. For example, to achieve roughly 20-nm spatial resolution, a sample size of about 60 μm is useful (Vega et al. 2013). For core-sized samples, greater voxel size is needed. In this work, we seek to measure the core-scale porosity distribution of tight, gas-bearing rocks where saturation with water is not practical. Saturation of samples with gas that provides sufficient attenuation to apply Eq. (1) does appear to be practical, however. For example, Lu et al. (1992) used a dual-scan technique with a single energy, as proposed by Moss et al. (1992), to calculate porosity using Eq. (1). They used krypton gas as the radio-opaque agent and determined porosity of Devonian shale samples. Moss et al. (1992) went on to measure dual-porosity distributions of Monterey and Bakken shale as well as coal using xenon for contrast. Lu et al. (1994) also examined Devonian shales to determine gas storage under dynamic flow conditions. Watson and Mudra (1994) characterized Devonian shales with X-ray tomography also using xenon and Eq. (1). Coal was the subject sample of study for Karacan and Okandan (1999). In their work, they used xenon and dual-energy CT scanning to visualize flow and estimate storage capacity.

3 Pore Microstructure

Although the intent of this study is to understand the distribution of porosity at about the 0.1-mm scale in cm-sized samples, it is important to consider smaller scales. Advanced imaging

technologies are employed widely for microstructural studies of gas shales and coal. This section reviews briefly relevant results and conceptual models.

Ambrose et al. (2010) proposed a petrophysical model that summarizes the volumetric constituents of shale matrix. In the model, a bulk volume encompasses the total rock mass, and it is subdivided into void and nonvoid volumes. Within the total void volume, sorbed gas, free gas, and isolated pore volume are delineated. The nonvoid volume is formed of clay, nonclay, and organic matter. It is widely accepted that shale is composed of an inorganic and an organic matrix with varying degrees of interconnection. The presence of microfractures that facilitate connection between the matrices is speculated among researchers.

The storage capacity of gas shales is widely considered to reside within its organic matrix, also referred to as kerogen. Most efforts have estimated the kerogen matrix size, distribution, pore size, and porosity and connectivity. Elgmati et al. (2011) studied Haynesville and Utica shale samples, finding calcite-healed fractures, pyrite framboids surrounded by clay platelets, as well as nanoporosity within pyrite framboids. They used focused ion beam (FIB) milling to obtain 200 slices of Fayetteville shale that were examined with scanning electron microscopy (SEM). They stacked the slices together to obtain a three-dimensional pore model, reporting a rock porosity of 3.34 % and kerogen porosity of 40–50 %. Curtis et al. (2010) performed FIB/SEM on 300–600 slices of a shale sample also to reconstruct the images into a 3D model. They mention kerogen porosities of up to 50 % being previously reported by Sondergeld et al. (2010). In their study, they classified porosities into "crack-like" (much like the microcracks that connect inorganic and organic matrices), phyllosilicate (triangular and linear and located in the inorganic matrix between clay particles), and organophyllic (kerogen-related, round porosity with dimensions on the order of nm). Similar to Elgmati et al. (2011), they also observed that organophyllic porosity was often associated with pyrite in the shale, both in framboid and in individual crystal forms, as well as with apatite.

Sondergeld et al. (2010) report that most of the pores they imaged were found in minerals, organics, and microcracks and in pyrite framboids. Later, Curtis et al. (2011) reported kerogen imaged with scanning tunneling electron microscopy (STEM) from Barnett shale samples to be "sponge-like" in appearance. Samples showed a certain degree of connection in their internal structure, and estimates of porosity were around 14.4 %. They also imaged Haynesville shale samples for which they found significant porosity in the inorganic matrix (~6.2 %) that was identified as phyllosilicate porosity. Curtis et al. (2011) are uncertain whether thermal maturity plays a role in the amount and diversity of organophyllic porosity. On the other hand, Wang and Reed (2009) reported kerogen porosities to be less than 25 %.

We turn briefly to the microstructure of coal. Coal pore structure is heterogeneous and varies with coal type and rank (Laxminarayana and Crosdale 1990). Coalbeds are often characterized by two distinctive porosity systems: a uniformly distributed network of natural fractures and porous blocks between the cleats (King et al. 1986). The natural fractures (also known as cleats) are subdivided into face and butt cleats. The face cleat is continuous throughout the reservoir, whereas the butt cleat is discontinuous and terminates at intersections with the face cleat. The cleat spacing is uniform and ranges from the order of millimeters to centimeters (King et al. 1986).

The heterogeneous pore structure of coal and shale offers pore sizes varying from a few Angstroms to over a micrometer in size. According to the IUPAC classification (1994), pores may be classified into macropores (>50 nm), transient or mesopores (between 2 and 50 nm), and micropores (<2 nm). Determination of pore volumes and their distribution in coals and shale is important to understand the storage and gas transport behavior of gases such as CO_2, CH_4 and/or N_2 (Rice 1993; Clarkson and Bustin 1999; Shi and Durucan 2008)

Table 1 Comparison of image-calculated and database-estimated[a] porosities for the examined samples

Sample	Depth (ft.)	Image-calculated ϕ (%)	Estimated ϕ (%)
Barnett	8,562.10	6.50	5–6
Haynesville	11,283.90	6.40	5–7
	10,661.55	3.71	2.42
	11,102.45	1.40	2.77
Eagle Ford	12,753.30	4.80	5–7

[a] Estimates as provided by the service company that prepared core samples

4 Samples

Both coal and shale samples were used. A group of gas shale core samples from the Barnett, Haynesville, and Eagle Ford formations was used in this work. The field sample plugs were 1 inch (2.5 cm) diameter and approximately 2 inches (5.1 cm) in length and were cut parallel to bedding. Sample porosity was estimated to be between 2 and 7 % (Table 1). Clay content varies between 27 and 39 %. TOC ranges between 3.75 and 5.76, approximately. One of the Barnett samples displays a set of two calcite-filled fractures that run lengthwise along the core. Dark gray colored, the samples do not show any other visible markings.

The coal originates from a coalbed at a depth of 900–1,200 feet (270–370 m) below the ground surface. It came from the Wyodak-Anderson group of the Powder River Basin. Average in-situ pressure and temperature were estimated between 360 and 500 psi (2,500–3,400 kPa) and 28 to 32 °C, respectively. The coal sample as received was not preserved at formation conditions, but was extensively fractured and broken into cm-sized pieces. It was filled with formation water and contained some clay or shale.

5 Experimental

The experimental setup consisted of apparatus, core holders, and X-ray CT scanners as detailed next.

5.1 X-ray CT

Two CT scanner machines were used. The shale imaging was done on a GE HiSpeed CT/i fifth generation medical scanner operated in helical mode. The voxel dimension is 0.25 by 0.25 by 1 mm, the tube current is 120 mA, and the energy level of the radiation ranges from 80 to 120 keV. For the coal study, a Picker 1200 SX fourth generation scanner with 1200 fixed detectors was employed. The scanner operates in axial mode. The voxel dimension is 0.4 by 0.4 by 3 mm, the tube current is 125 mA, and the energy level of the radiation is 130 keV. The X-ray exposure for one image is 4 s, while the processing time is about 40 s. The images obtained with both scanners display sufficient contrast among rock features and do not exhibit detectable positioning errors because of the large energy level and positioning system, respectively. An example resolution from the CT/i machine is shown in Fig. 1. The fine grid indicates voxel dimension projected in two dimensions, and raw CT numbers are presented.

5.2 Gases

X-ray CT, as employed here, provides a fraction of a millimeter spatial resolution to measure porosity. Equation (1) demands sufficient contrast between scans of the sample filled with

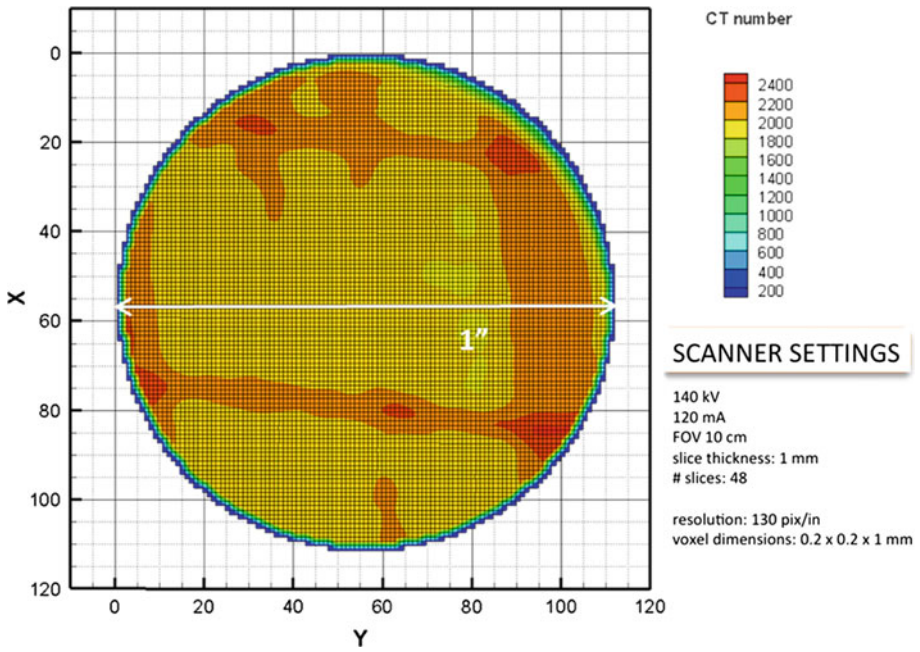

Fig. 1 GE HiSpeed CTi X-ray CT scanner image resolution details for shale samples

two different fluids. Hence, gases that exhibit significant attenuation at the energy levels obtainable in our CT systems are needed. We use xenon for coal and krypton for shale experiments.

Xenon has been previously used to model natural gas (methane) in coal (Karacan and Okandan 1999) and is our choice for coal studies in this paper. On the other hand, krypton gas has been used as the saturating fluid for Devonian shales (Lu et al. 1992) because of some similarities with natural gas, such as Lennard-Jones potential constant, polarizability, and van der Waals radii. Lu et al. (1992) also speculate that krypton and methane may have similar storage properties on porous solids, so results found with krypton may be translated (potentially) to natural gas estimates. Additionally, factors to choose krypton gas for our studies were that kinetic diameters of krypton and CO_2 are 0.3685 and 0.33 nm, respectively, and krypton gas provides significant contrast in attenuation as compared to vacuum, nitrogen, or air. Figure 2 shows the CT numbers (H) of bulk krypton versus pressure (psi) and X-ray tube energy (keV) obtained in the CT/i scanner.

5.3 Shale Apparatus

A coreholder system compatible with the reservoir material and the X-ray CT scanner was designed, fabricated, and tested. The core samples were placed between two stainless steel end caps that contain fluid distribution channels that allow for gas circulation across the sample faces. The end caps provide access to a confining pressure system and to a pore pressure system. The samples were coated with a high temperature epoxy compound (730 Solvent Resistant Sealant, Dow Corning) and sleeved with heat-shrinkable Teflon (PTFE HS 2:1 Heat Shrink, Zeus). The core sleeve isolates the core from the confining fluid and allows realistic confining stress to be applied. The net effective stress applied to the samples

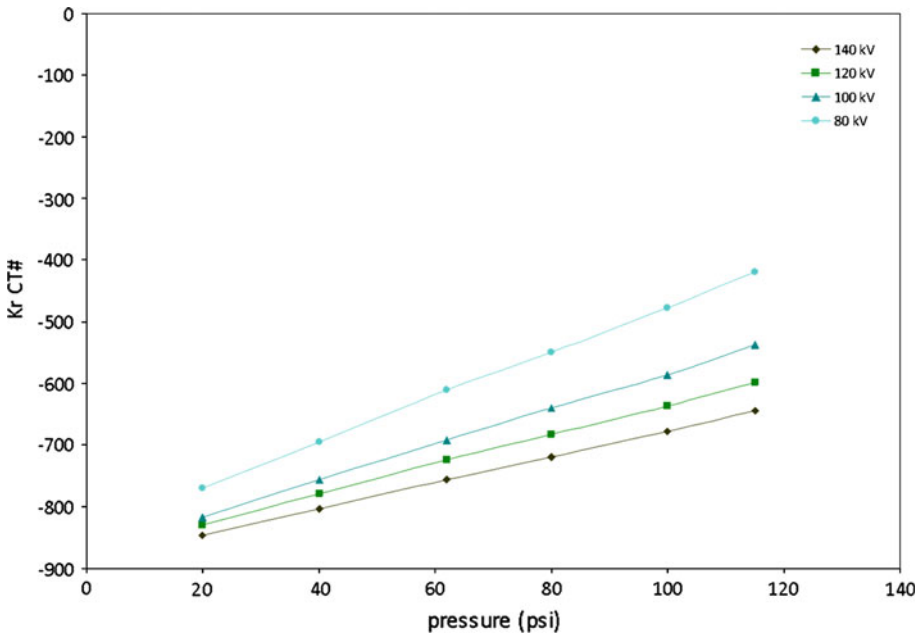

Fig. 2 CT number of krypton gas versus pressure and CT scanner energy

was roughly 150–200 psi (1,000–1,400 kPa). An outer 1/6" thick aluminum sleeve slides over the core and seals via o-rings on the end caps. Threaded aluminum rods pass through the end caps and serve to hold the entire apparatus together when subjected to pressure. The apparatus is able to withstand pressures up to approximately 2,000 psi (14,000 kPa). A sketch of the experimental setup is presented in Fig. 3. The assembled coreholder was oriented horizontally.

An experiment proceeds by first placing the core in a vacuum oven and heating to 70 °C until the weight of the sample stabilizes. The core is then jacketed (as described above) and placed in the coreholder. Confining pressure is applied. A vacuum pump is then used to remove any gas from the core. Gas injection occurs such that gas travels lengthwise toward the production end of the core. The injection pressure is 100 psi (690 kPa). The valve at the production end is closed such that steady flow does not occur but rather pressure stabilization is sought. This mode of operation conserves the relatively expensive krypton. Pressure transducers send data to an acquisition system. Pressure stabilization is achieved when the pressure at the production end equals the injection pressure. The core is evacuated using the vacuum pump for subsequent experiments.

5.4 Coal Apparatus

To establish that gas transport is potentially measured by monitoring the movement of radio-opaque agents, we proceeded to transient gas flow in coal. Coal matrix is less tight and less dense allowing greater ease of measurement. A second coreholder system compatible with our objective of imaging transient gas flow was constructed out of PVC and tested. Figure 4 shows a schematic of the apparatus and illustrates the scan plane. A conventional viton rubber sleeve is used to jacket the coal. For these studies, the entire length of the sample

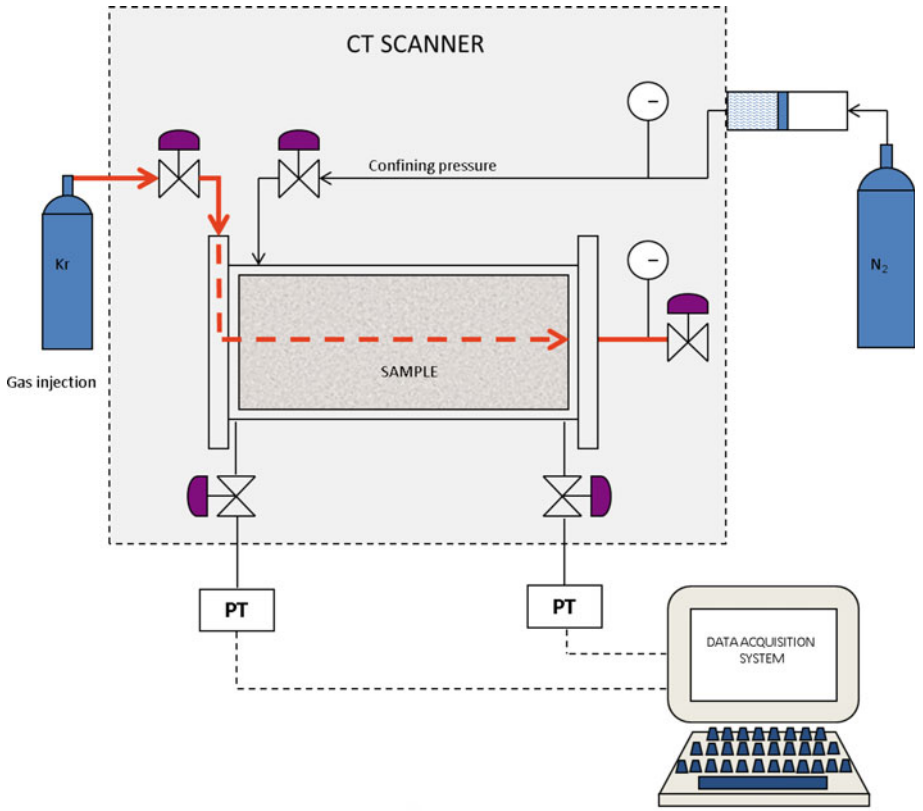

Fig. 3 Shale imaging apparatus

is scanned rather than cylindrical cross sections. The relatively low density of PVC and the fact that the coreholder does not need to be translated improve our ability to image transient gas flow. The unconventional scan geometry, however, tends to increase the frequency of artifacts in the CT scan images. The water jacket placed around the core holder has a circular cross section and eliminates artifacts, see the discussion of coreholder design in Akin et al. (2000) and Akin and Kovscek (2003). The water jacket also aids in maintaining constant temperature.

To prepare the apparatus, coal was dried in a vacuum oven at 30 °C until its weight stabilized and then stored in a vacuum desiccator. Three separate cylindrical pieces of coal were stacked on top of each other, and ground coal was placed between each piece to allow better alignment as a composite cylinder. The gaps between pieces mimic cleats and fractures in coal. Then, the coal pieces were wrapped in foil, stacked in the core sleeve, and placed in the core holder. The bulk dimensions of the composite core were 1 in diameter by 3 in long (2.5 by 9.5 cm). The apparatus was connected to a vacuum pump to evacuate any air or moisture that the pieces may have picked up during assembly for approximately two weeks. Once thoroughly evacuated, the core holder was inserted vertically in the water jacket chamber and flushed with N_2 at 15 psia (103 kPa). N_2 at 70 psia also serves as the confining pressure. After sealing the whole assembly, the water jacket is filled with water. The core holder is closed at one end (no flow/flux boundary), while the penetration of xenon into the

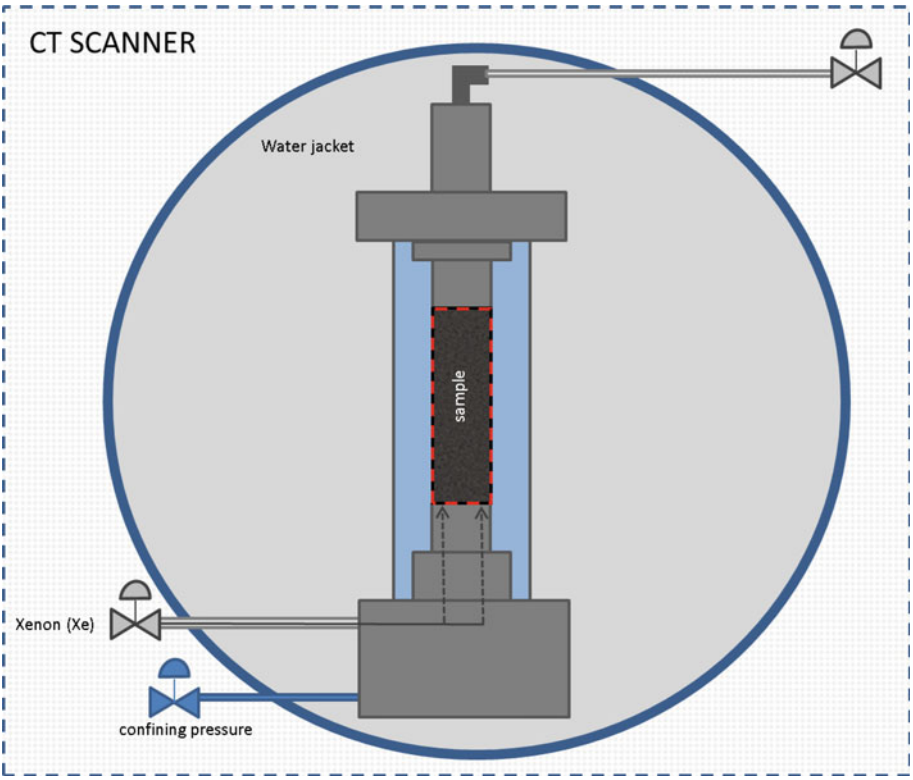

Fig. 4 Coal imaging apparatus. The *dashed box* illustrates the approximate position of a portion of the composite core that is imaged

coal was carried out by exposing the other end (base of core holder) to xenon at a pressure of 15 psia (103 kPa). CT images were collected periodically as the xenon penetrated the coal.

6 Results and Discussion

The experimental results are discussed with shale porosity distributions first and transient gas transport in coal second.

Figure 5 shows the principle of the porosity calculation. An evacuated and then gas-saturated sample is scanned, and a number of cross-sectional slices are obtained. The cross-sectional images are then subtracted to obtain the difference in mass coefficient attenuation of the two states (represented by the CT number). The resulting group of images highlights the pore space penetrated by the gas and porosity follows from Eq. (1). These images, when reconstructed in three dimensions, depict the spatial distribution of porosity within the sample, as illustrated in Figs. 5 and 6.

Several shale samples were subjected to similar experiments. Varying results were obtained in achieving pressure stabilization of the gas injected in the samples due to low permeability and heterogeneity. An example of one result with krypton injection in a Barnett core sample is shown in Fig. 6. Although microporosity and microfractures are present in the sample (Vega et al. 2013), such details are averaged into the porosity (structural details) that we

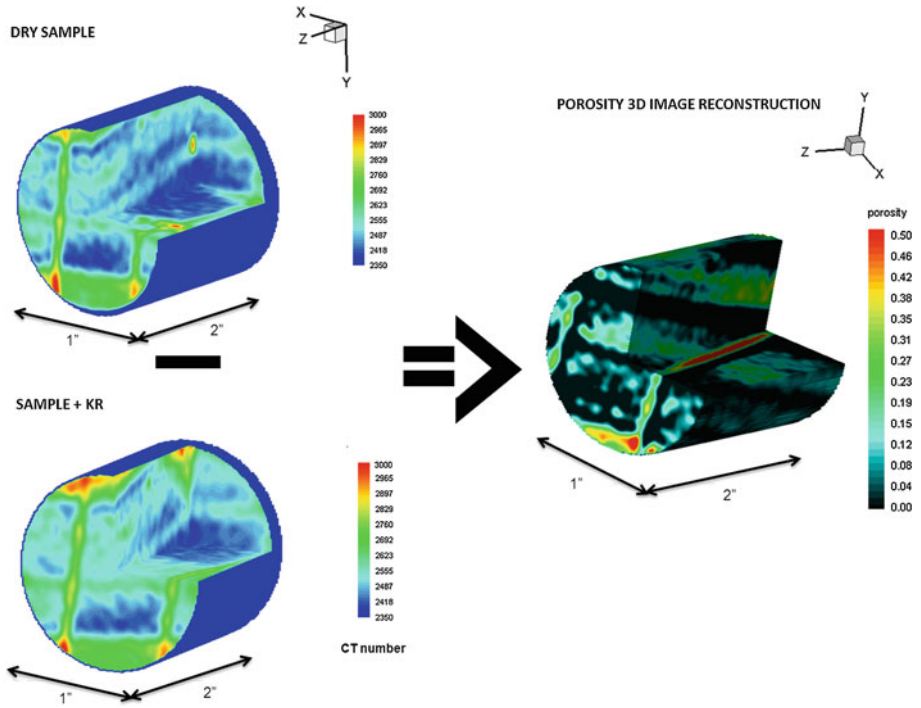

Fig. 5 Image subtraction principle used to estimate porosity of a gas shale sample using CT images

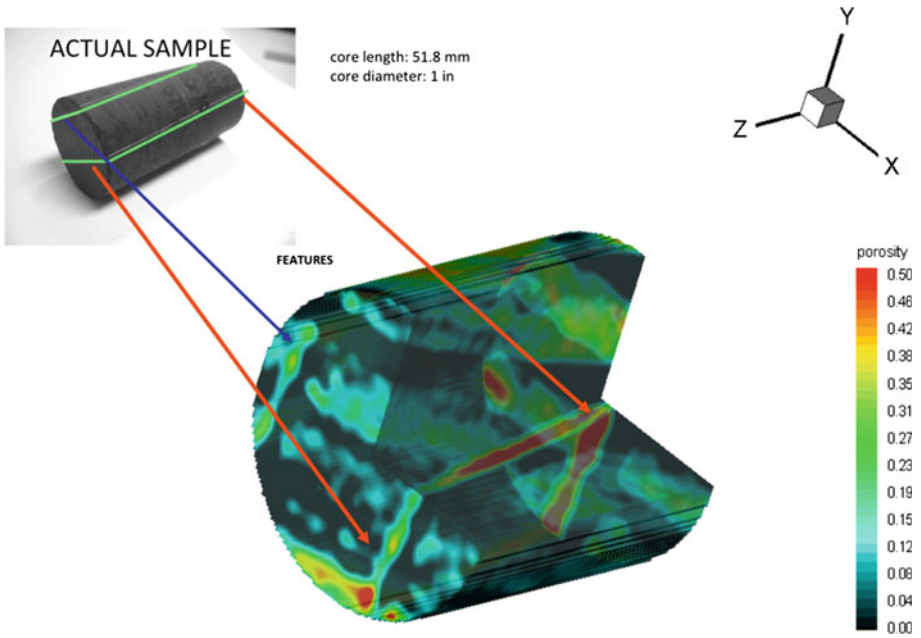

Fig. 6 Three-dimensional porosity map reconstruction obtained for Barnett sample

measure for each voxel. Red shading indicates a porosity of 0.5, whereas black is 0. Calcite-filled fractures are apparent during visual inspection of the sample and in the reconstructed porosity map. Matrix material adjacent to the fracture is also evident. Average calculated porosity for the sample was 6.5 % (Table 1). Fractures that appeared to be healed or cemented closed (presumably with calcite) are outlined in green in the photograph of the core in Fig. 6. These fractures seem to have larger porosity than the rest of the matrix and are permeable to krypton because of an imperfect filling of the fractures or opening of the fracture in the drilling/coring process. Core heterogeneity and bedding are clearly demonstrated in Figs. 5 and 6.

The 3D in-situ porosity images may be analyzed statistically. Figure 7 shows the frequency (i.e., number of counts) of appearance of a particular porosity and gives a map of the three-

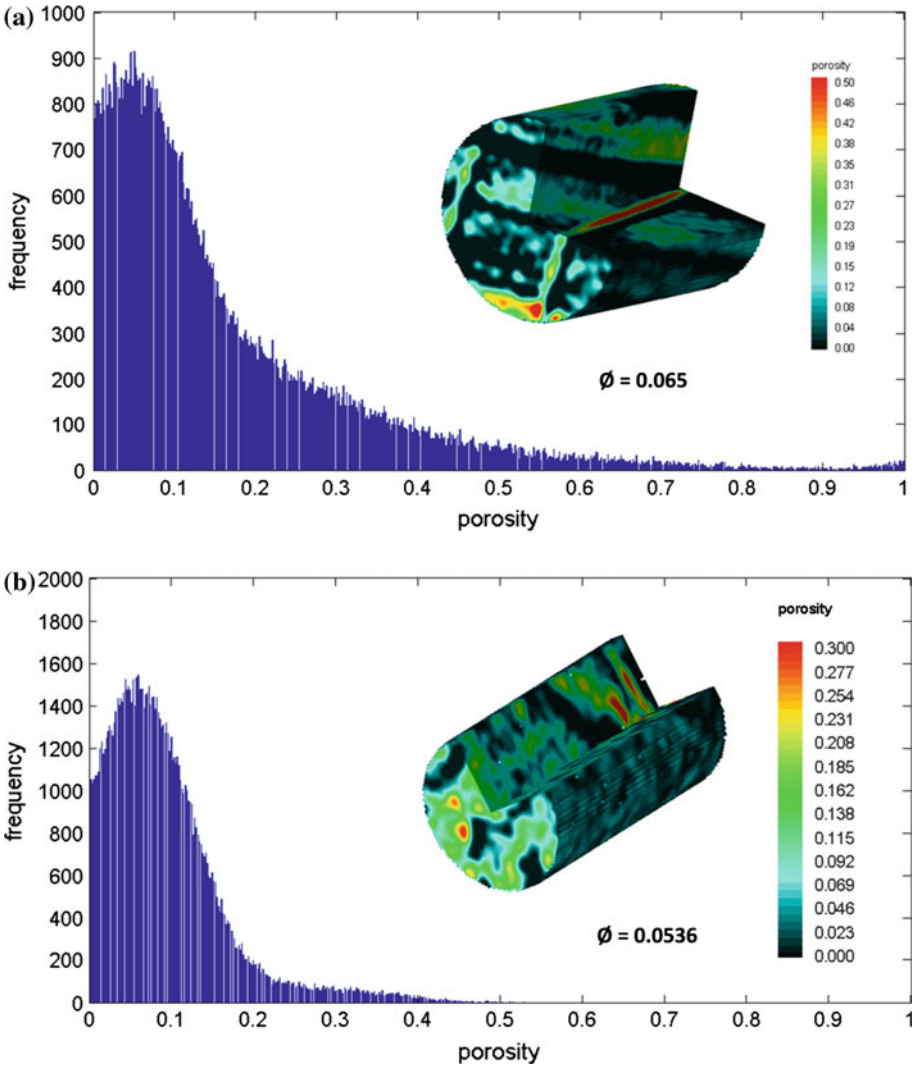

Fig. 7 Porosity distribution for two of the samples represented in this study: **a** Barnett and **b** Eagle Ford

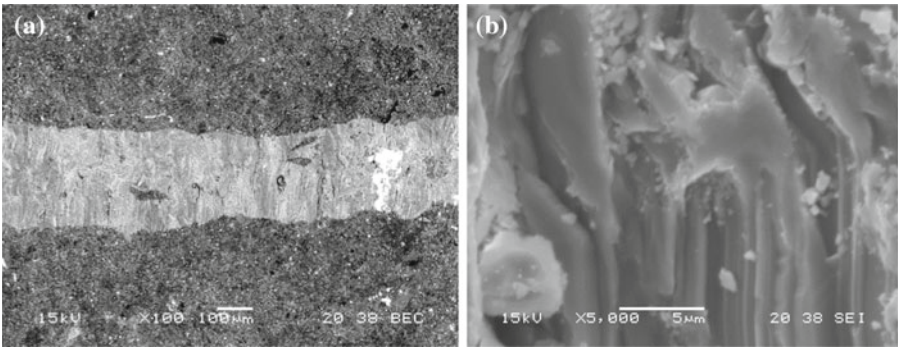

Fig. 8 SEM–BSE images of the calcite-filled fracture on the Barnett sample (courtesy of C. Ross). **a** 100× and **b** 5,000×. The fracture fill in **b** is oriented identical to that in **a**

dimensional porosity distribution as an inset, Barnett (a) and Eagle Ford (b). The Eagle Ford sample has an average porosity of 0.054, but there is a long tail of greater porosity values. The average porosity of the core by CT scanning is obtained by summing the porosity measured in each voxel and dividing by the number of voxels. About 9 % of the porosity measurements are greater than 0.15, but a significant fraction (43 %) of the measured values are 0 as well.

The Barnett sample, Figs. 6 and 7a, also has a long tail of fairly large porosity values that mostly originate from the fracture. The fracture and calcite filling were investigated using SEM and a small piece of the end trim from the core. Figure 8 shows the SEM images (courtesy of C. Ross) of the calcite. The first SEM–BSE image in Fig. 8a shows the light gray (calcite) fracture surrounded by dark matrix. Bright white areas in the fracture are sulfate minerals such as barite, and the white areas in the matrix are pyrite. The image in Fig. 8b is a close up view showing small pores and voids in the calcite fracture fill. These along with other images (not shown) support the higher porosity found in the fracture fill via krypton CT images.

Figure 6 also shows evidence of bedding structures in the sample, with at least three visible and alternating smaller and larger porosity distribution areas. The black shaded volumes have zero porosity, according to CT measurements. In volumes of the core with nonzero porosity, porosity is in the range of 15 %. These nonzero porosity regions may be connected kerogen, and we are working on their identification. The central part near the cemented fracture has porosity in excess of 50 %. These high porosities are in a very small volume and may represent incomplete cementing of the fracture.

To establish that the high X-ray contrast gas technique is widely applicable, additional samples were analyzed following the procedures given above. Figure 9 shows additional porosity maps of unfractured Haynesville samples. Distinct features are observed such as regions of larger porosity distributed within a small porosity matrix. Differences in the porosity distributions of these three samples are apparent on these maps, and the average porosity values calculated through Kr injection reasonably match the porosity values estimated for the samples from related databases or otherwise measured with methods such as He pycnometry.

A comparison of the estimated porosity values with porosity values obtained from other sources for some of the samples is offered in Table 1. The heterogeneity of each core is clearly apparent as is the tortuous path followed by krypton in order to saturate the cores. These results are consistent with theories of a dispersed, medium–low-porosity matrix within a connected, low-porosity inorganic matrix. However, evidence of microfractures was not found for the

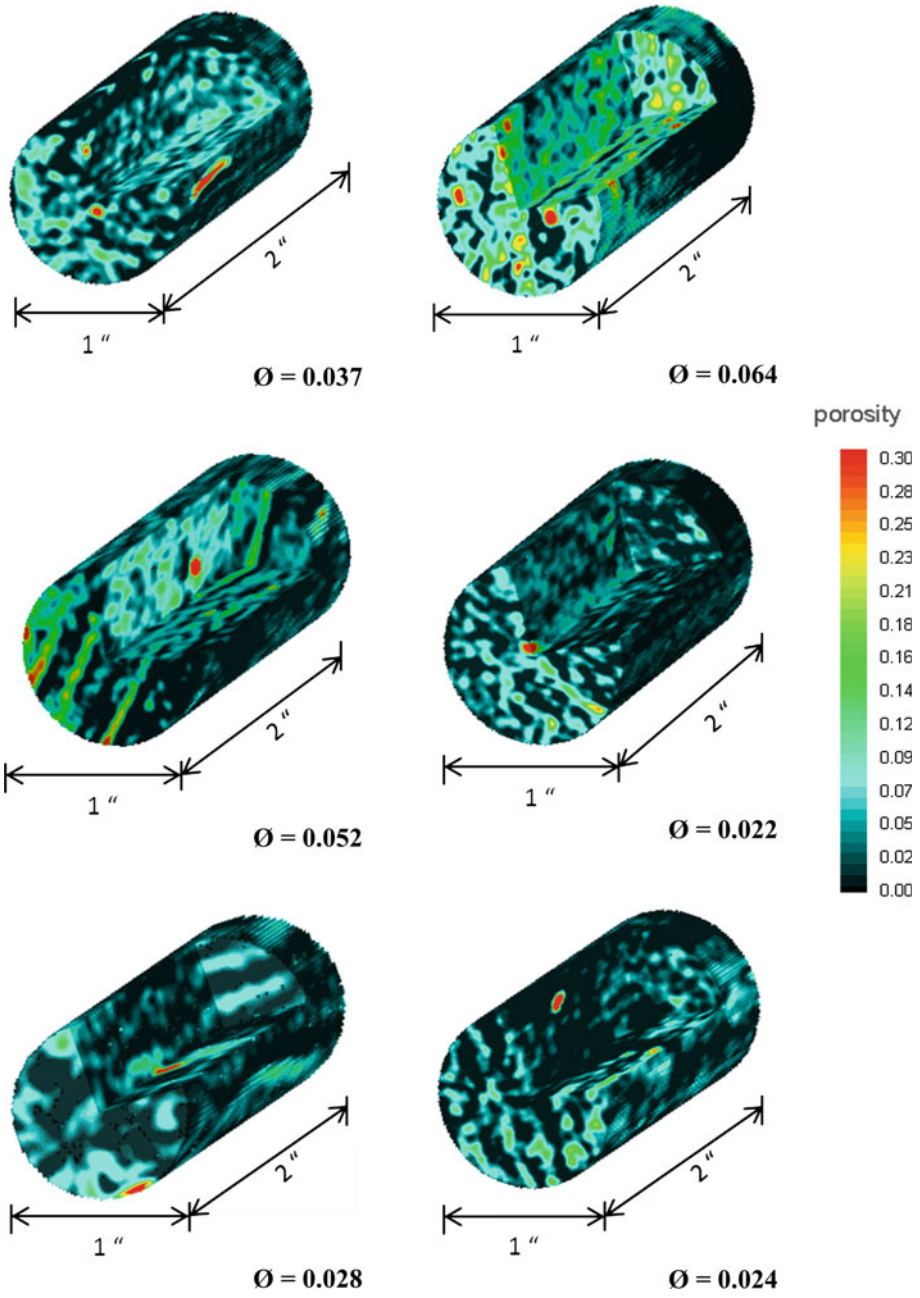

Fig. 9 Three-dimensional porosity map reconstruction obtained for six additional Haynesville samples

image resolution of these studies, probably due to a mismatch of scales between the equipment (submillimeter) and the probable size of these features (microns to nanometers).

For experiments that determine porosity distribution, it does appear that adequate contrast in attenuation is available between vacuum and krypton-saturated images. This result is

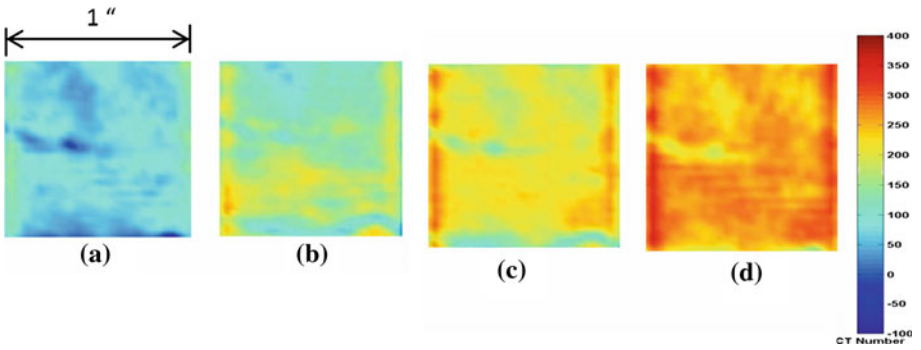

Fig. 10 CT scan images of the central coal piece shown by the *dashed box* in Fig. 4 at **a** $t = 0$ min, **b** $t = 51$ min, **c** $t = 8$ h 33 min, and **d** $t = 44$ h

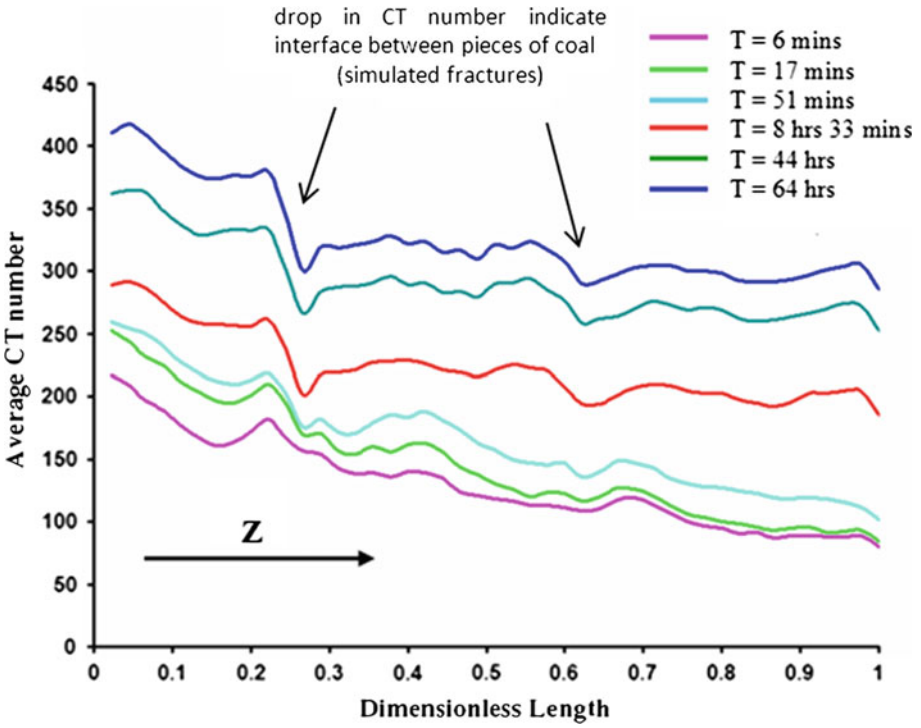

Fig. 11 CT number variation along the length of coal sample with time as xenon diffuses into the matrix. Boundaries of coal pieces are called out with *arrows*

encouraging as computations using the beginning and end state result in insightful images. An additional goal of this work is to establish that gas transport is measureable by monitoring the progress of radio-opaque agents through porous media. For this demonstration, we use coal, xenon, and the apparatus shown in Fig. 4.

With time, xenon gas flows into the coal matrix, and as a result, its concentration in the coal matrix increases as shown in Fig. 10. The experiment was allowed to run for 44 h to enable adequate penetration of the porous medium. Figure 10a–d are the CT scan images

for the middle coal piece in the composite core at different times. From these images, one observes the slow penetration of xenon into the coal. Hence, this experimental study captured the dynamic transport of xenon via CT scan images. An increase in CT number with time implies a proportional increase in the xenon concentration in coal. As a result, the variation of CT number along the length of coal at different times is representative of the xenon concentration profile as a function of time.

Next, the CT numbers along the horizontal plane were averaged for each axial location to obtain 1D profiles. Figure 11 shows the average CT number variation for a particular location with time along the length of coal. It is clear that as the concentration of xenon builds up inside the coal pack over time, the CT number increases. We suggest that through application of proper experimental boundary conditions, the CT measurements allow one to monitor diffusive transport of gas in situ. Because the change in CT number with time is proportional to the increase in xenon concentration, it is possible to obtain an estimate of diffusion coefficient (Dutta 2009).

7 Summary

Imaging of the porosity distribution within low-permeability media was accomplished and enhanced by implementing a high X-ray contrast gas imaging technique. The method uses X-ray CT imaging of the sample of interest under vacuumed and tracer gas-saturated stages. Imaging of the gas-accessible pore space is possible through an image subtraction algorithm. It is thus possible to obtain submillimeter resolution images and 3D reconstructions that represent the average porosity spatial distribution of the sample.

Gas shale rock imaging was performed with X-ray computed tomography (CT scanning). Porosities calculated with krypton injection in shale matched approximately the porosities predicted for samples of similar origins or measured through different means. Calcite-filled fractures were observed with the naked-eye and submillimeter resolutions. These fractures displayed larger porosity values than the rest of the shale. Krypton injection combined with CT scanner imaging seems to produce enough signal to be detectable and achieve reasonable porosity values with this nondestructive technology. Large, connected low-porosity areas enveloping spotted, medium–low-porosity zones consistently appear in the sample porosity maps studied. This observation supports theories of medium–low-porosity organic matrices dispersed within low, connected inorganic matrices as the probable pore network distribution for gas shale rocks similar to the subjects of the study.

The experimental study on coal focused on the use of X-ray CT for imaging gas flow in coal. The pore structure of coal and diffusion phenomenon of a gas inside coal was examined by injecting xenon gas into coal at room temperature (25 °C). Xenon was chosen because of its relatively inert nature and because it is a strong attenuator at the X-ray energies available to us. Differential rates of mass transport involving diffusion and advection were measurable from the CT scans, and these provided evidence of the heterogeneous nature of the coal dual-porosity pore structure. The increase in xenon concentration observed through the increase in CT numbers with time occurred primarily via a diffusion mechanism. Fractures simulated through the interface between the coal pieces stacked together were also observable and proved to be a major gas transport distributor to the coal matrix, as evidenced by the CT number behavior within the sample.

Acknowledgments A portion of this work was prepared with the support of the US Department of Energy under Award No. DE-FE-0004731. However, any opinions, findings, conclusions, or recommendations

expressed herein are those of the authors and do not necessarily reflect the views of the DOE. Additional financial support was provided by the Stanford University Petroleum Research Institute (SUPRI-A) Industrial Affiliates. We also acknowledge C. Ross who provided SEM analysis of the Barnett core sample.

References

Akin, S., Schembre, J.M., Bhat, S.K., Kovscek, A.R.: Spontaneous imbibition characteristics of diatomite. J. Pet. Sci. Eng. **25**, 149–165 (2000)

Akin, S., Kovscek, A.R.: Computed Tomography in Petroleum Engineering Research. Applications of X-ray Computed Tomography in the Geosciences. Geological Society, London, Special Publications, 215, pp. 23–28 (2003)

Akkutlu, Y., Fathi, E.: Multi-scale gas transport in shales with local Kerogen heterogeneities. Paper SPE 146422 presented Annual Technical Conference and Exhibition held in Denver, CO. 30 Oct–2 Nov (2011)

Ambrose, R.J., Hartman, R.C., Diaz-Campos, M., Akkutlu, Y., Sondergeld, C.H.: New Pore-scale considerations for shale gas in place calculations. Paper SPE 131772 presented at the SPE Unconventional Gas Conference held in Pittsburgh, PA, 23–25 Feb (2010)

Clarkson, C.R., Bustin, R.M.: The effect of pore structure and gas pressure upon the transport properties of coal: a laboratory and modeling study. 2. Adsorption rate modeling. Fuel **78**, 1345–1362 (1999)

Curtis, M.E., Ambrose, R.J., Sondergeld, C.H., Rai, C.S.: Structural characterization of gas shales on the micro- and nano-scales. Paper SPE 137693 presented at the Canadian Unconventional Resources & International Petroleum Conference held in Calgary, Canada, 19–21 Oct (2010)

Curtis, M.E., Ambrose, R.J., Sondergeld, C.H., Rai, C.S.: Transmission and scanning electron microscopy investigation of pore connectivity of gas shales on the nanoscale. Paper SPE 144391 presented at the SPE North American Unconventional Gas Conference and Exhibition held in The Woodlands, TX, 14–16 Jun (2011)

Dutta, A.: Multicomponent gas diffusion and absorption in coals for enhanced methane recovery. Master thesis report, Stanford University (2009)

Elgmati, M., Zhang, H., Bai, B., Flori, R., Qu, Q.: Submicron-pore characterization of shale gas plays. Paper SPE 144050 presented at the SPE North American Unconventional Gas Conference and Exhibition held in The Woodlands, TX, 14–16 Jun (2011)

Harris, J, Kovscek, A.R., Orr, F.M., Zoback, M.D.: Geologic storage of carbon dioxide. Technical Report of the Global Climate and Energy Project, Stanford University. http://gcep.stanford.edu/research/technical_report/20012.html (2008)

Honarpour, M.M., Cromwell, V., Hatton, D., Satchwell, R.: Reservoir rock descriptions using computed tomography (CT). Paper SPE 14272 presented at the SPE Annual Technical Conference and Exhibition held in Las Vegas, NV, 22–25 Sep (1985)

IPCC.: Special report on carbon dioxide capture and storage. Ch. 5: underground geological storage (2005)

IUPAC: recommendations for the characterization of porous solids. Pure Appl. Chem. **66**(8), 1739–1758 (1994)

Jessen, K., Tang, G.-Q., Kovscek, A.R.: Laboratory and simulation investigation of enhanced coalbed methane recovery by gas injection. Transp. Porous Media **73**(2), 141–159 (2008)

Kang, S.M., Fathi, E., Ambrose, R.J., Akkutlu, I.Y., Sigal, R.F.: Carbon dioxide storage capacity of organic-rich shales. Paper SPE 134583 presented at the Annual Technical Conference and Exhibition held in Houston, TX, 3–6 Oct (2010)

Karacan, C.O., Okandan, E.: Heterogeneity effects on the storage and production of Gas from coal seams. Paper SPE 56551 presented at the Annual Technical Conference and Exhibition held in Florence, Italy, 19–22 Sep (1999)

King, G.R., Ertekin, T., Schwerer, F.: Numerical simulation of the transient behavior of coal-seam degasification wells. SPE Formation Evaluation **2**(1), 165–183 (1986)

Laxminarayana, C., Crosdale, P.J.: Role of coal type and rank on methane sorption characteristics of Bowen Basin, Australia. Int. J. Coal Geol. **40**, 309–325 (1990)

Le Guen, S.S., Kovscek, A.R.: Non-equilibrium effects during spontaneous imbibition. Transp. Porous Media **63**, 127–146 (2006)

Lin, W., Tang, G.-Q., Kovscek, A.R.: Sorption-induced permeability change of coal during gas-injection processes. SPE Reserv. Eval. Eng. **11**(4), 792–802 (2008)

Lu, X.C., Pepin, G.P., Moss, R.M., Watson, A.T.: Determination of gas storage in Devonian shales with X-ray-computed tomography. Paper SPE 24810 presented at the 67th Annual Technical Conference and Exhibition held in Washington, DC, 4–7 Oct (1992)

Lu, X., Miao, P., Watson, A.T., Pepin, G.P., Moss, R.M., Semmelbeck, M.: X-ray computerized tomography studies of gas storage and transport in Devonian shales. AIChE J. **40**(7), 1246–1253 (1994)

Moss, R.M., Pepin, G.P., Davis, L.A.: Direct measurement of the constituent porosities in a dual-porosity matrix. Log Analyst. **33**(2), 126–135 (1992)

Nuttall, B., Drahovzal, J., Eble, C. Bustin, R.: Analysis of Devonian black shales in Kentucky for potential carbon dioxide sequestration and enhanced natural gas production. Final Report to U.S. Department of Energy. http://www.osti.gov/scitech/biblio/920185 (2005)

Rice, D.D.: Composition and origins of coalbed gas. In: Law, B.E., Rice, D.D. (eds) Hydrocarbons from Coal. AAPG Studies in Geology, 38, 159–185 (1993)

Saites, F, Wang, G., Guo, R., Mannhardt, A., Kantzas, A.: Coalbed characterization studies with X-ray computerized tomography (CT) and micro CT techniques. Paper 2006–027 presented at the Canadian International Petroleum Conference held in Calgary, Canada, 13–15 Jun (2006)

Shi, J.Q., Durucan, S.: Modeling mixed-gas adsorption and diffusion in coalbed reservoirs. SPE 114197, paper presented at the SPE Unconventional Reservoirs Conference held in Keystone, CO (2008)

Sondergeld, C.H., Ambrose, R.J., Rai, C.S.: Micro-structural studies of gas shales. Paper SPE 131771 presented at the SPE Unconventional Gas Conference held in Pittsburgh, PA, 23–25 Feb (2010)

Vega, B., Andrews, J.C., Liu, Y., Gelb, J., Kovscek, A.R.: Nanoscale visualization of gas shale pore and textural features. In: Proceedings of the Unconventional Resources Technology Conference held in Denver, Colorado, USA, 12–14 Aug (2013)

Vinegar, H.J., Wellington, S.L.: Tomographic imaging of three-phase flow experiments. Rev. Sci. Instrum. **58**, 96–107 (1987)

Wang, F.P., Reed, R.M.: Pore networks and fluid flow in gas shales. Paper SPE 124253 presented at the Annual Technical Conference and Exhibition held in New Orleans, LA, 4–7 Oct (2009)

Watson, A.T., Mudra, J.: Characterization of devonian shales with X-ray computed tomography. SPE Form. Eval. **9**(3), 209–212 (1994)

Whithjack, E.M.: Computed tomography for rock property determination and fluid flow visualization. Soc. Pet. Eng. Form. Eval. **3**, 696–705 (1988)

Whithjack, E., Devier, C., Michael, G.: The role of X-ray computed tomography in core analysis. Paper SPE 83467 presented at the SPE Western Regional/AAPG Pacific Section Joint Meeting held in Long Beach, CA, 19–24 May (2003)

Wong, S., Gunter, W.D., Mavor, M.J.: Economics of CO_2 sequestration in coalbed methane reservoirs. SPE 59785, presented at the 2000 SPE/CERI Gas Technology Symposium held in Calgary, Alberta Canada (2000)